Riblets in the Rough Regime

L. H. von Deyn[1], M. T. Hehner[1], J. Serpieri[1], J. Kriegseis[1], D. Gatti[1] and B. Frohnapfel[1]

[1] *Institute of Fluid Mechanics, Karlsruhe Institute of Technology, Karlsruhe, Germany*
von-deyn@kit.edu

July 19, 2021

Abstract

Riblets of triangular shape are experimentally investigated with emphasis on the drag-increasing regime in an air turbulent channel flow facility. The nondimensional riblet spacing s^+ and height h^+ in viscous units are varied by changing the bulk Reynolds number in the range $5 \times 10^3 < Re_b < 8.5 \times 10^4$. The change in skin-friction drag is accurately measured by comparing the pressure drop across the test section with smooth and ribbed walls at given values of Re_b. Stereoscopic particle image velocimetry (sPIV) is used to obtain velocity data in the cross plane up to $Re_b = 3.7 \times 10^4$. The measurements show that riblets, in the drag-increasing regime, depart from the the typical "k"-type roughness in the fully-rough regime. Via the sPIV measurements, the emergence of wall-normal velocity above the riblet tips was detected when increasing Re_b to the drag increasing regime. This could be an indication that secondary flows play a role for the breakdown of the drag-reducing regime of riblets, experimentally supporting the findings of Modesti et al. (2021).

1 Introduction

Riblets are one of the few proven possibilities to reduce the skin-friction drag in turbulent flows and, therefore, have been extensively studied in the past, e.g. Bechert et al. (1997).

It is known that the spanwise spacing s of the riblet crests determines the presence and amount of drag reduction. When scaled in viscous units $s^+ = s\, u_\tau/\nu$ (i.e. made nondimensional by the wall friction velocity u_τ of the flow and the kinematic viscosity ν of the fluid) an optimal spacing of $s^+ \approx 15$ was found Bechert et al. (1997).

The drag-increasing regime of riblets is much less studied in the literature. Jiménez (2004) hypothesized that riblets in their drag-increasing regime behave like classical "k"-type roughness. However, Gatti et al. (2020) showed that, for triangular riblets, such a regime exists, but, when further increasing Re_b (bulk Reynolds number $Re_b = 2\, U_b\, \delta/\nu$ defined with the effective half-channel height δ), the amount of drag increase is lower compared to the value expected from a "k"-type roughness prediction.

The underlying mechanisms for this behavior remain unknown. In general, little is known about the reasons for the breakdown of the drag-reducing regime of riblets. Endrikat et al. (2021) conducted an extensive numerical study on various riblet shapes investigating the influence of Kelvin–Helmholtz (KH) instabilities on the drag-reduction breakdown. While some configurations (e.g. steep $30°$ tip-angle sawtooth riblets) show a significant contribution of KH instabilities to drag, other shapes/angles of riblets do not reveal a contribution of KH rollers. Therefore, KH-related flow mechanisms are significant for the breakdown of the drag-reducing regime, but alone do not provide the explanation. Modesti et al. (2021) analysed the effect of secondary flows on the drag penalty of riblets using the same numerical dataset Endrikat et al. (2021) . Interestingly, the emergence of secondary flows occurs as the drag induced by the riblets increases. Thus, further analysis of secondary flows as a cause for the breakdown of the drag-reducing regime and/or of the experimentally-proven deviation from "k"-type roughness seems promising.

In the current study, we present experimental data on two riblets sets in a bulk-Reynolds number range of $3 \times 10^3 < Re_b < 8.5 \times 10^4$ with the intent to clarify the behavior of riblets in the drag-increasing regime, experimentally complementing the findings of Gatti et al. (2020). Additionally, the adopted sPIV measurements enable the analysis of velocity profiles and of secondary flows.

2 Methodology

The experimental investigations are carried out in an open-circuit blower tunnel Güttler (2015). The facility allows the measurement of small changes in skin-friction drag by evaluating the static pressure at 21 pressure taps located along both side walls of a $314\,\delta$-long channel test section with an aspect ratio of 1:12. The test sec-

tion is divided into three segments of $76\,\delta$, $119\,\delta$ and $119\,\delta$ streamwise extents. In the present investigation, the last segment is equipped with two sets of riblets with the characteristics shown in table 1. For this purpose, a high-precision milling machine was used to manufacture the desired surfaces. A photography of the *sawtooth* riblets is shown in figure 1. The facility allows to vary the bulk Reynolds number within the range of $5 \times 10^3 < Re_b < 8.5 \times 10^4$.

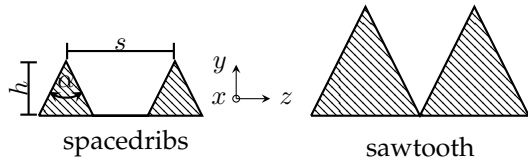| ID	s [mm]	h [mm]	α [°]	δ [mm]
spacedribs	0.614	0.294	53.5	12.49
sawtooth	1	0.87	60	12.375

Table 1: Overview of the investigated riblet geometries.

The streamwise pressure gradient Π, assessed via the 0.3 mm static pressure taps spaced 200 mm in streamwise direction, is employed to evaluate the global wall-shear stress τ_w. The effective half-channel height δ, used as the length scale throughout the manuscript, is defined based on the concept of a (streamwise) parallel protrusion height $h_\parallel$ Luchini et al. (1991). Thus, the wall-normal origin is placed $h_\parallel$ below the riblet tip and was computed based on the analytic expressions provided by Bechert and Bartenwerfer (1989) who solved the underlying Stokes flow problem via conformal transformations.

In combination with the mass flow rate $\dot{V}$, measured with an orifice flow meter with interchangeable orifice plates, the skin friction coefficient C_f, defined through $C_f = \frac{2\,\tau_w}{U_b^2 * \rho}$, can be deduced. Changes in ambient conditions are accounted for by tracking the wind tunnel air temperature and the ambient pressure and humidity.

Figure 1: Photography of the *sawtooth* riblets.

In order to resolve streamwise (u), wall-normal (v) and spanwise velocity (w) components, complementary sPIV measurements are carried out. The measurement plane captures a cross-section of the flow $3.5\ \delta$ upstream of the test-section outlet. Two Photron SA4 high-speed cameras at the left and right side of the channel exit, positioned at approximately $28°$ with respect to the streamwise direction, are used to take particles (1 μm diameter Di-Ethyl-Hexyl-Sebacate droplets) images. Lenses with a focal length of $200\,\text{mm}$ and an aperture of $f/8$ are used in conjunction with a 2x-teleconverter for each lens and mounted on Scheimpflug adapters fitted to accommodate the viewing angles. The cameras are operated in double-frame mode (sampling frequency $480\,\text{Hz}$) at full sensor size ($1024 \times 1024\,\text{px}$) and a spatial resolution of about 60 px/mm. The particles are illuminated by a Quantronix Darwin-Duo Nd:YLF laser that accesses the channel test section through a convex lens window on the side wall, used to align the light sheet parallel to the wall, thus minimizing reflection issues from the walls. The light sheet thickness is set to $0.5\,\text{mm}$ corresponding to ≈ 30 px. A laser pulse distance of $12\,\mu\text{s}$ (repetition rate $240\,\text{Hz}$) is adopted for $Re_b = 1.8 \times 10^4$ to reach a maximum displacement in the streamwise direction of 10 px. The streamwise displacement was kept constant for the investigated values of Re_b stated in table 2, thus the pulse distance was accordingly adjusted to reach the desired $1/3$ displacement with respect to the laser light-sheet thickness. The raw images were cross-correlated on a final interrogation window size of 48×16 px with an overlap factor of $50\,\%$. Further details on the sPIV experimental set-up can be found in Hehner et al. (2021).

$Re_b \times 10^4$	0.5	1.2	1.8	2.85	3.7
smooth-wall	○	x	□	△	◇
spacedribs		x	□	△	◇
sawtooth	○	x	□	△	◇

Table 2: sPIV-investigated flow cases. The symbols are used in figure 4.

3   Results

The skin-friction coefficient C_f vs. the bulk Reynolds number Re_b is presented in figure 2 (Nikuradse-type diagram), where the measurements obtained on both riblet sets and the smooth surface are included (compare table 1). For reference, the correlation proposed by Dean is included alongside the smooth-wall data Dean (1978). For the *spacedribs* riblets, the expected drag reduction compared to the smooth-wall ref-
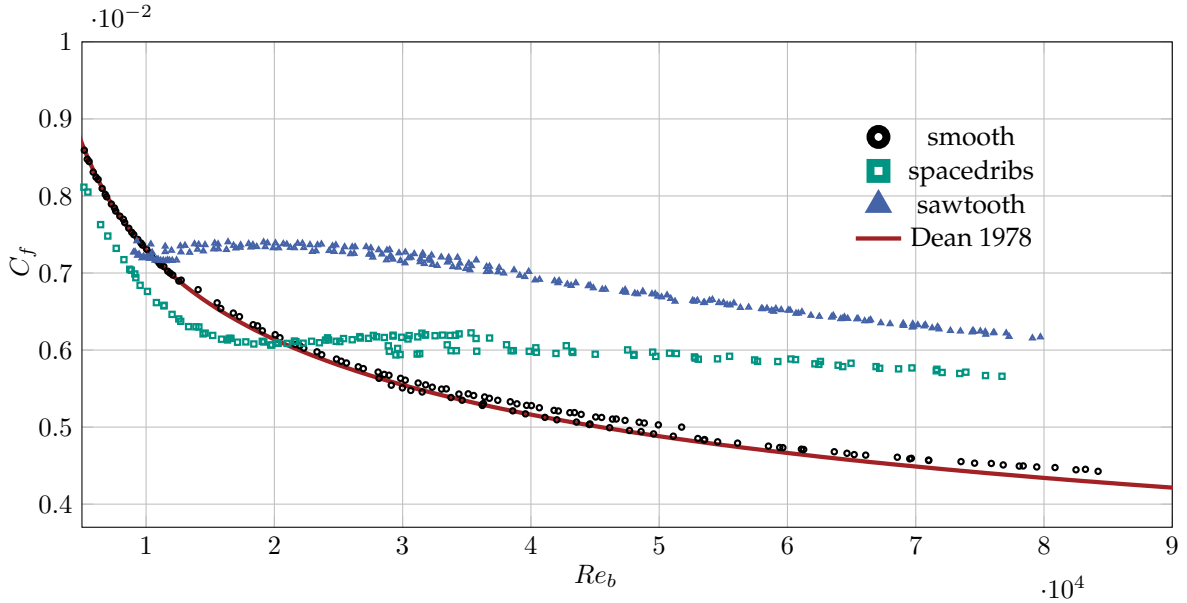
Figure 2: Nikuradse-type diagram for the investigated riblet geometries. Smooth-wall data and Dean correlation Dean (1978) included for reference.

erence is evident with an optimum at $Re_b \approx 1.2 \times 10^4$ (corresponding to $s^+ \approx 15$). Due to the larger physical size of the *sawtooth* riblets, the drag-reducing regime is reached at the low end of the Re_b-range of the windtunnel around $Re_b \approx 1 \times 10^4$. Both sets show a consistent behaviour in the rough regime: A fully rough surface would tend to a constant skin-friction coefficient from a certain Re_b onward (dependant on the individual roughness). Both riblet sets, however, reveal a broad Re_b region of almost constant C_f followed by a C_f decrease with increasing Re_b, thus not reaching a fully rough behaviour in the current measurement range. This decrease in C_f is more pronounced for the *sawtooth* riblets which have a larger physical size. Considering the 2-D character of the riblet geometries, hence lacking any pressure drag, the lack of a fully rough regime is somewhat expected. Gatti et al. (2020) discuss the roughness behaviour for the *spacedribs* riblets and their deviation from a "k"-type roughness behaviour in detail. The present additional measurement data for physically larger *sawtooth* riblets nicely confirm this skin-friction drag behavior of riblets in the rough regime.

For the local analysis of the velocity data obtained from sPIV measurements, a different approach is taken to extract the wall-shear stress τ_w (i.e. u_τ) expressed in viscous units: Instead of the global pressure drop along the streamwise direction, the wall-normal total stress obtained from sPIV measurements is fitted and evaluated at the wall-normal origin ($h_\parallel$ below the riblet tip). The total stress and its contributions are exemplary shown in figure 3 for the highest drag-reduction
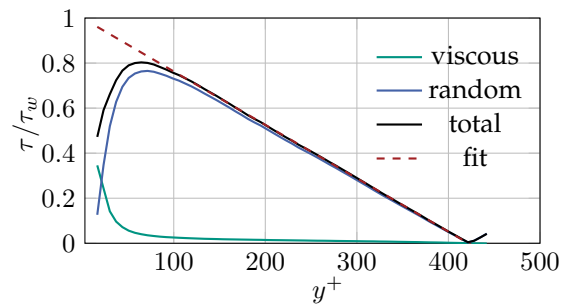

Figure 3: Total stress contributions for *spacedribs* riblets at $Re_b = 1.2 \times 10^4$. The fit (red dashed line) is used to extract the wall-shear stress τ_w.

case *spacedribs* riblets at $Re_b = 1.2 \times 10^4$. In the bulk region, the expected linear trend of the total stress is visible also proving the statistical convergence of the sPIV results. Closer to the wall (figure 3) $y^+ < 100$), the limitations of the near-wall resolution cause a deviation from the linear behaviour. Thus, data from this region are discarded for the fit.

Additionally to the shown C_f measurements, the riblet's global effect on the turbulent flow can be assessed analysing the mean streamwise velocity profiles in viscous units as shown in figure 4. The profiles are shown for all cases listed in table 2 (markers defined there). A smooth-wall DNS at $Re_\tau = u_\tau \delta / \nu = 2000$ is included for reference Hoyas and Jiménez (2008). Consistent trends between the pressure-drop results presented in figure 2 and the velocity profiles are found: The shift of the riblet's velocity profile
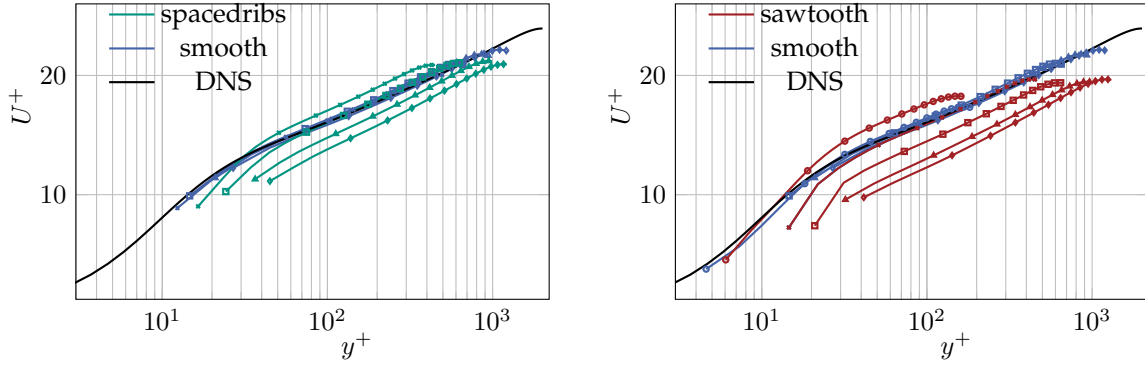
Figure 4: U^+ vs. y^+ for *spacedribs* and *sawtooth* riblets in comparison to smooth-wall velocity distribution from the sPIV measurements. Markers indicate different Re_b as specified in table 2. Smooth-wall DNS at $Re_\tau = 2000$ included for reference Hoyas and Jiménez (2008).
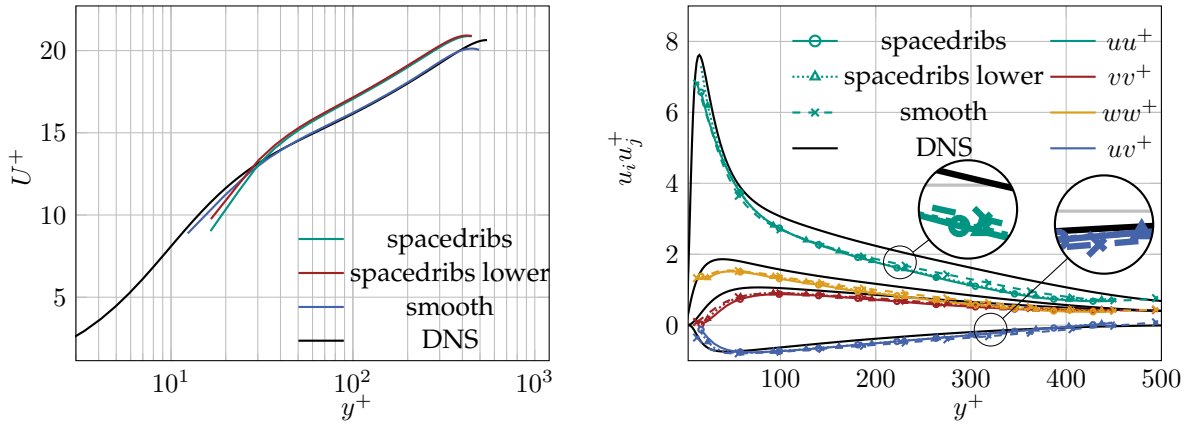

Figure 5: Reynolds stresses $u_i u_j^+$ vs. y^+ for *spacedribs* riblets at $Re_b = 1.2 \times 10^4$ in comparison to smooth-wall sPIV data. Left panel: Smooth-wall DNS at $Re_\tau = 550$ included for reference Hoyas and Jiménez (2008). "lower" refers to a non-symmetric channel: lower channel side equipped with a riblet plate, top of the channel smooth surface.

with respect to the smooth-wall reference case ΔU^+ also quantifies the amount of drag reduction/increase. E.g. in the left panel of figure 4, the upward shift of the riblet profile for $Re_b = 1.2 \times 10^4$ stems from the drag-reducing effect of the riblets while with increasing Re_b the riblet's velocity profiles tend to a bigger shift. Quantitatively, the drag increase/reduction $\Delta C_f / C_{f0}$ derived from sPIV measurements deviates less then 5 % from the pressure-drop measurements.

Figure 5 shows the velocity- and Reynolds stress profiles for *spacedribs* riblets at $Re_b = 1.2 \times 10^4$ (highest drag reduction case). Here, two configurations are shown for the same riblet geometry: The term "lower" refers to a non-symmetric channel where the lower channel side was equipped with a riblet plate; while the top of the channel had a smooth surface. These results are presented alongside the "normal" symmetric configuration, where top and bottom walls of the channel are equipped with riblets (as in all the other presented cases). From figure 5 it is evident

that the asymmetric configuration does not effect neither the averaged statistics of streamwise velocity u nor the relevant Reynolds stresses. Compared to the smooth-wall case, only slight differences can be detected when considering the Reynolds stresses (right panel of figure 5): As expected, uu^+ and uv^+ are slightly smaller compared to the smooth-wall case due to the drag reducing effect of the riblets. Again, DNS data by Hoyas and Jiménez (2008) is included for reference. In general, a good match between the profiles for smooth-wall mean velocity and Reynolds stress profiles is found.

Spanwise- wall-normal contours of the wall-normal velocity component v for all riblet cases are shown in figure 6, here normalized with the centerline velocity U_{Cl}. On the left side of figure 6, the results for *spacedribs* riblets (the physically smaller riblets) are shown. Re_b increases from top to bottom. For *spacedribs* riblets, where all measurements were conducted in or close to the drag-reducing regime (in terms of Re_b), no
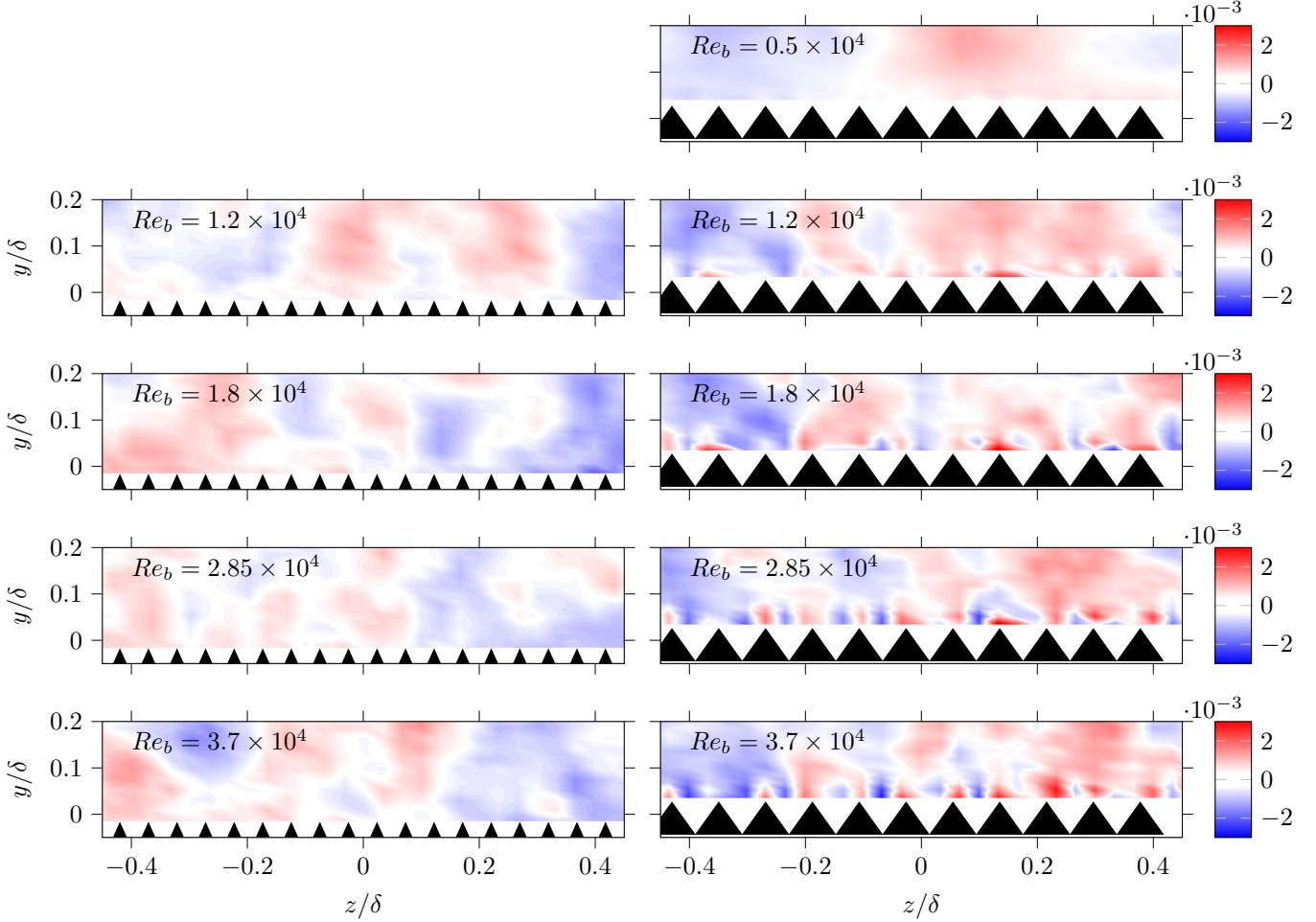
Figure 6: Time-averaged V/U_{Cl} contours for *spacedribs* (left) and *sawtooth* (right) riblets.

vertical velocity in the riblet's near region can be detected. A different picture arises in case of the *sawtooth* riblets: With increasing Re_b, an increasing V/U_{Cl} magnitude in the riblet vicinity is detected: Above the riblet's tip, fluid is moved upwards, while in the valley fluid pushed downwards. This observation indicates the emergence of secondary motions as the riblet's drag penalty increases. It is worth noting that the small physical size of the riblets poses a significant challenge for the measurement equipment. The visible time-averaged contour levels at some distance from the wall stem from nonphysical artefacts in the processing. Due to the very small intensity of the secondary flow ($V/U_{Cl} \approx 0.2\%$), the mean streamwise particle displacement is 3

orders of magnitude larger compared to the inplane motion. Thus, experimental detection of such secondary flows is hard to achieve. Yet, the presented results show clear evidence of the presence of secondary flows in the riblets' vicinity in agreement with the numerical findings of Modesti et al. (2021).

The joint analysis of the Reynolds-number dependence of the wall-friction and secondary motions appears to be a promising approach to shed further light on a possible explanation for the observed friction behaviour.

4 Conclusions

Two sets of riblets installed in a fully-developed turbulent channel flow were investigated experimentally via pressure-drop and sPIV measurements. The obtained skin-friction coefficient C_f reveals the expected $\approx 8\%$ drag reduction at $s^+ \approx 15$. With increasing Re_b, the riblet's drag-reducing regime breaks down while C_f does not reach a fully-rough state, at least in the investigated range up to $Re_b < 8.5 \times 10^4$. The obtained changes in C_f are confirmed by the sPIV measurements, i.e the the shift of the streamwise velocity profiles in viscous units ΔU^+ matches the pressure-drop measurement results. An effect of an asymmetric channel flow on the velocity- and Reynolds-stress profiles could be ruled out by comparing sPIV measurements of a symmetric (riblets on lower and upper channel wall) and asymmetric (riblets only on the lower wall, upper wall smooth) configuration. In order to gain an understanding of the observed C_f vs. Re_b behaviour, the wall-normal velocity fields in the vicinity of the riblet tips were analysed. This revealed the emergence of secondary flow motions with increasing roughness (i.e. drag-increasing) effect of the riblets as recently shown by Modesti et al. (2021) numerically. The approach of simultaneously performing skin-friction measurements and local analysis of the secondary flows can possibly contribute to the understanding of the riblets' drag-reducing regime breakdown.

Acknowledgments

References

Bechert D.W. and Bartenwerfer M. (1989). The viscous flow on surfaces with longitudinal ribs. *Journal of Fluid Mechanics*, 206:105–129. ISSN 1469-7645, 0022-1120.

Bechert D.W., Bruse M., Hage W., Hoeven J.G.T.V.D., and Hoppe G. (1997). Experiments on drag-reducing surfaces and their optimization with an adjustable geometry. *Journal of Fluid Mechanics*, 338:59–87. ISSN 1469-7645, 0022-1120.

Dean R.B. (1978). Reynolds Number Dependence of Skin Friction and Other Bulk Flow Variables in Two-Dimensional Rectangular Duct Flow. *Journal of Fluids Engineering*, 100(2):215–223. ISSN 0098-2202.

Endrikat S., Modesti D., García-Mayoral R., Hutchins N., and Chung D. (2021). Influence of riblet shapes on the occurrence of Kelvin–Helmholtz rollers. *Journal of Fluid Mechanics*, 913. ISSN 0022-1120, 1469-7645.

Gatti D., von Deyn L., Forooghi P., and Frohnapfel B. (2020). Do riblets exhibit fully rough behaviour? *Experiments in Fluids*, 61(3):81. ISSN 1432-1114.

Güttler A. (2015). High accuracy determination of skin friction differences in an air channel flow based on pressure drop measurements.

Hehner M.T., von Deyn L.H., Serpieri J., Pasch S., Reinheimer T., Gatti D., Frohnapfel B., and Kriegseis J. (2021). Stereo piv of oscillatory plasma discharges in the cross plane of a channel flow. *14th International Symposium on Particle Image Velocimetry (ISPIV 2021),August 1–5, 2021.*

Hoyas S. and Jiménez J. (2008). Reynolds number effects on the reynolds-stress budgets in turbulent channels. *Physics of Fluids*, 20(10):101511.

Jiménez J. (2004). Turbulent Flows Over Rough Walls. *Annual Review of Fluid Mechanics*, 36(1):173–196.

Luchini P., Manzo F., and Pozzi A. (1991). Resistance of a grooved surface to parallel flow and cross-flow. *Journal of Fluid Mechanics*, 228:87–109. ISSN 1469-7645, 0022-1120.

Modesti D., Endrikat S., Hutchins N., and Chung D. (2021). Dispersive stresses in turbulent flow over riblets. *Journal of Fluid Mechanics*, 917. ISSN 0022-1120, 1469-7645.